Research Article

# Layer-controlled 2D Sn$_4$P$_3$ via space-confined topochemical transformation for enhanced lithium cycling performance

Jianan Gu[1], Yongzheng Zhang[2] (✉), Bingbing Fan[1], Yanlong Lv[1], Yanhong Wang[1], Ruohan Yu[3] (✉), and Meicheng Li[1] (✉)

[1] State Key Laboratory of Alternate Electrical Power System with Renewable Energy Sources, School of New Energy, North China Electric Power University, Beijing 100096, China
[2] State Key Laboratory of Chemical Engineering, East China University of Science and Technology, Shanghai 200237, China
[3] Wuhan University of Technology, Sanya 572000, China

## ABSTRACT

Topochemical transformation has emerged as a promising method for fabricating two-dimensional (2D) materials with precise control over their composition and morphology. However, the large-scale synthesis of ultrathin 2D materials with controllable thickness remains a tremendous challenge. Herein, we adopt an efficient topochemical synthesis strategy, employing a confined reaction space to fabricate ultrathin 2D Sn$_4$P$_3$ nanosheets in large-scale. By carefully adjusting the rolling number during the processing of Sn/Al foils, we have successfully fabricated Sn$_4$P$_3$ nanosheets with varied layer thicknesses, achieving a remarkable minimum thickness of two layers (~ 2.2 nm). Remarkably, the bilayer Sn$_4$P$_3$ nanosheets display an exceptional initial capacity of 1088 mAh·g$^{-1}$, nearing the theoretical value of 1230 mAh·g$^{-1}$. Furthermore, we reveal their high-rate property as well as outstanding cyclic stability, maintaining capacity without fading more than 3000 cycles. By precisely controlling the layer thickness and ensuring nanoscale uniformity, we enhance the lithium cycling performance of Sn$_4$P$_3$, marking a significant advancement in developing high-performance energy storage systems.

## KEYWORDS

topochemical transformation, 2D materials, confined reaction, layer-controlled, Sn$_4$P$_3$ nanosheets, lithium storage

## 1   Introduction

Recent advancements in materials science have brought two-dimensional (2D) materials into the limelight, thanks to their distinctive physical, chemical, and electronic attributes [1–6]. Demonstrating considerable promise in diverse applications including energy storage, semiconductors, and energy conversion, a variety of strategies have been devised for synthesizing 2D materials [7–13]. These approaches are principally categorized into two main pathways: the top-down method, which includes liquid or mechanical exfoliation, and the bottom-up method, encompassing techniques such as chemical vapor deposition (CVD) or the van der Waals epitaxy approach [14–19].

The synthesis strategies for 2D materials hold significant importance due to their critical role in overcoming the challenges associated with fabricating these materials. However, synthesizing 2D materials often presents substantial hurdles, including controlling layer thickness, uniformity, and composition at the nanoscale [20–23]. For instance, the exfoliation method frequently produces nanosheets with varying thickness and numerous by-products, limiting its precision [24–27]. Conversely, methods such as CVD or van der Waals epitaxy offer some control over thickness by adjusting reaction times, temperatures, and quantities of reactants but are hampered by low yield and high energy demands, which curtail their broader application [28–31].

Topochemical transformation has emerged as a potent method for fabricating 2D materials with precise control over their composition and morphology [32, 33]. This approach leverages a solid-state reaction within a 2D plane, transforming precursors into layered structures with high precision. Topochemical synthesis distinguishes itself by its ability to produce high-purity materials with substantial mass and controlled phase composition, thereby opening new avenues for the synthesis of 2D materials while maintaining the integrity of the layered structure [34, 35]. Despite these advancements, the large-scale synthesis of ultrathin 2D materials with controllable thickness remains a daunting challenge [36]. This limitation significantly impacts the performance of 2D materials in practical applications, especially in fields like energy storage and catalysis, where precise material characteristics are crucial for efficiency and effectiveness.

Herein, we adopt a pioneering and efficient topochemical synthesis strategy, employing a confined reaction space to fabricate ultrathin 2D Sn$_4$P$_3$ nanosheets in large-scale. By carefully adjusting the rolling number during the processing of Sn/Al foils, we have successfully fabricated Sn$_4$P$_3$ nanosheets with varied layer thicknesses, achieving a remarkable minimum thickness of roughly two layers (~ 2.2 nm). Remarkably, the bilayer Sn$_4$P$_3$ nanosheets display an exceptional initial capacity of 1088 mAh·g$^{-1}$, nearing the theoretical value (1230 mAh·g$^{-1}$). Furthermore, we

reveal their high-rate property as well as outstanding cycle life, maintaining capacity without fading more than 3000 cycles. By precisely controlling the layer thickness and ensuring nanoscale uniformity, we enhance the lithium cycling performance of $Sn_4P_3$, marking a significant advancement in the development of its practical application.

## 2    Experimental

### 2.1    The synthesis of bilayer, three-layer, and four-layer $Sn_4P_3$ nanosheets

Initially, Al and Sn foils were subjected to repeated folding and rolling using a rolling machine. By varying the number of rolling processes, nanosheets of different thicknesses were produced, with the bilayer $Sn_4P_3$ nanosheets being rolled 27 times, three-layer $Sn_4P_3$ nanosheets being rolled 20 times, and four-layer $Sn_4P_3$ nanosheets being rolled 15 times. Subsequently, these Al-Sn stacked nanosheets underwent phosphorization through a simple hydrothermal method using red P powder at 200 °C for 40 h in an ethanediamine solvent. This process allowed the resulting $Sn_4P_3$ to retain its 2D morphology, originally derived from Sn nanosheets, due to the confinement of the reaction within the 2D plane by the metallic Al nanosheets. Finally, the $Sn_4P_3$ nanosheets were acquired by etching the previously mentioned Al nanosheets in 0.1 M HCl aqueous solution, followed by several washes with deionized water and ethanol.

### 2.2    Morphological and structural characterization

The morphology and microstructure of these samples were comprehensively analyzed using a range of techniques. Atomic force microscopy (AFM) provided detailed surface topography and texture information. High-angle annular dark-field scanning transmission electron microscopy (HAADF-STEM) was conducted on a FEI Themis Z. Transmission electron microscopy (TEM) and selected area electron diffraction (SAED) examinations were conducted on a Tecnai G2 F20 U-YWIN system, offering insights into the nanoscale structure and arrangement of these materials. X-ray diffraction (XRD) measurements were conducted with a Rigaku D/max2500PC, utilizing Gu K$\alpha$ radiation, over a range of 20° to 70°, to verify the crystalline structure as well as phase composition of these samples. Additionally, Raman spectroscopy was used to assess the vibrational properties of these samples, utilizing a Horiba JY

LaRAM ARAMIS Raman microscopy system. These comprehensive characterization techniques collectively provided a thorough understanding of the samples' physical and chemical properties.

### 2.3    Electrochemical measurements

Electrochemical tests were performed based on 2032 coin-type cells. The working electrodes were fabricated by blending active materials with acetylene black and polyvinylidene fluoride (PVDF) in a 7:2:1 weight ratio, which was then spread onto pure Cu foil (with an active material mass loading of ~ 0.7 mg·cm$^{-2}$). Pure Li foil and polypropylene (PP) film were used as the counter electrode and separator, respectively. The electrolyte was composed of a 1.0 M $LiPF_6$ in a mixture of ethylene carbonate:dimethyl carbonate (EC:DMC, 1:1 wt.%). Repeated discharge/charge tests were performed on a Land CT2001A across a broad range of current densities (50, 100, 200, 400, 800, 1600, 3200, and 6400 mA·g$^{-1}$), within a voltage window of 0.01 to 3.00 V. Electrochemical impedance spectroscopy (EIS) measurements were carried out using CHI 760E.

## 3    Results and discussion

As depicted in Fig. 1, the topochemical synthesis of bilayer $Sn_4P_3$ nanosheets involves three primary steps. Initially, Sn-Al stacking nanosheets are prepared through a repeated rolling and folding technique, wherein Sn and Al foils are rolled together 27 times using a roller press. Theoretically, this process can reduce the thickness of the Sn or Al to $2^n$ times based on their original thickness [37]. However, due to the varying ductility of the materials and the rolling process's limitations, achieving the theoretical thickness reduction is a challenge. By varying the number of rolling times ($n$ = 27, 20, and 15), we can produce a series of Sn nanosheets with different thicknesses. Subsequently, the resultant Al-Sn stacking nanosheets undergo a phosphorization process using a straightforward hydrothermal method with red phosphorus powder at 200 °C for 40 h in ethanediamine solvent (Fig. S1 in the Electronic Supplementary Material (ESM)). This topochemical transformation process allows the resulting $Sn_4P_3$ to maintain its 2D morphology, which is derived from Sn nanosheets, as the metallic Al nanosheets confine the reaction to a 2D plane. Finally, $Sn_4P_3$ nanosheets are obtained by etching away the Al nanosheets in a 0.1 M HCl aqueous solution (Fig. S2 in the ESM).

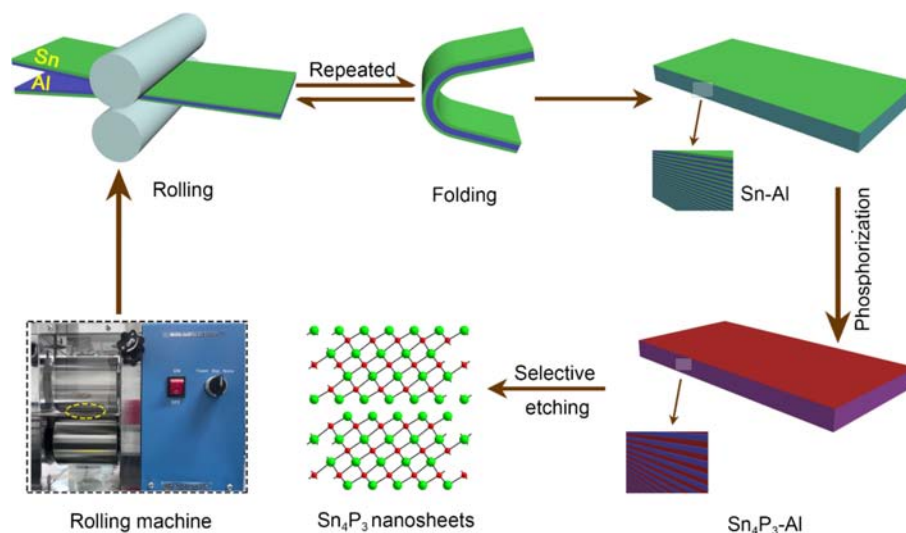The morphology and thickness of the synthesized nanosheets



**Figure 1**    Schematic illustration of the synthesis route for bilayer $Sn_4P_3$ nanosheets, which mainly involves three steps: repeated rolling and folding, phosphorization by confined reaction, and selective etching by 0.1 M HCl aqueous solution.

were first examined by TEM and HAADF-STEM measurements. TEM observations demonstrated the ultrathin nature of the bilayer $Sn_4P_3$ nanosheets, as illustrated in Fig. S3 in the ESM. Several foldable and transparent nanosheets were directly observable. High-resolution TEM (HRTEM) image (Fig. S4 in the ESM) showcased that the lattice spacing is 0.198 nm, matching the (110) facet belonging to $Sn_4P_3$. Additionally, HAADF-STEM images (Figs. 2(a)–2(d)) and the corresponding SAED patterns (Fig. S5 in the ESM) revealed a high-quality and single-crystalline hexagonal phase, akin to those observed in graphene and antimony [25], underscoring the high structural quality of these synthesized nanosheets. AFM measurements in Figs. 2(e) and 2(f), and Figs. S6 and S7 in the ESM vividly display a multitude of nanosheets, with sizes ranging from 0.4 to 0.8 μm, which could be intuitively observed. A statistical analysis of the thickness distribution of these nanosheets is presented in Fig. 2(g) and Table S1 in the ESM. The thicknesses of these nanosheets predominantly fall within the 2–3 nm range, accounting for 66.7% of the entire sample, aligning closely with the characteristics of bilayer $Sn_4P_3$ (2.236 nm). Notably, by fine-tuning the rolling number, we have successfully prepared nanosheets with varying thicknesses, corresponding to three-layer (Figs. S8–S10 in the ESM) and four-layer $Sn_4P_3$ (Figs. S11 and S12 in the ESM), demonstrating the capability to control the number of layers.

To verify the crystal structure of the prepared $Sn_4P_3$ nanosheets, XRD analysis was performed. The XRD pattern, depicted in Fig. 3(a), reveals distinct peaks at 28.7°, 30.2°, 31.4°, 44.4°, and 45.6°. These peaks correspond to the (015), (0012), (107), (0114), and (110) crystal facets of $Sn_4P_3$, respectively [38, 39]. Notably, the (110) crystal facet aligns with observations from HRTEM results previously discussed (Fig. S4 in the ESM). Additionally, the XRD spectra indicate that the bilayer $Sn_4P_3$ nanosheets exhibit significantly weaker intensity compared to their three-layer and four-layer counterparts (Fig. 3(b)). This reduction in intensity is attributed to the decreased thickness of the nanosheets, which results in diminished XRD signal strength. This observation is further supported by Raman spectroscopy analysis. As exhibited

in Fig. 3(c), the peak at 208 cm$^{-1}$ for bilayer $Sn_4P_3$ nanosheets is noticeably weaker in intensity when compared to those of the three-layer and four-layer $Sn_4P_3$ nanosheets. This trend is consistent with that observed in other exfoliated 2D nanomaterials, such as graphene and Sb nanosheets [25], where layer thickness has a pronounced effect on the intensity of spectral features, confirming the sensitivity of these techniques to changes in the structural dimensions of nanomaterials.

X-ray photoelectron spectroscopy (XPS) tests were conducted to confirm the element state of bilayer $Sn_4P_3$ nanosheets, as shown in Fig. 3(d). The absence of elements other than Sn, P, C, and O attests to the high purity of the bilayer $Sn_4P_3$ nanosheets. In the Sn 3d spectrum (Fig. 3(e)), four distinct peaks are observed, signifying the simultaneous presence of $Sn^{4+}$ and $Sn^{2+}$ states within the $Sn_4P_3$ structure. This coexistence indicates a complex valence state of Sn, contributing to the material's unique properties. Furthermore, the P 2p spectrum displays a notably broad peak around 134 eV, which corroborates the existence of P–O bonds. This finding suggests the formation of P–O bonds, possibly due to surface oxidation or the interaction of P with residual oxygen-containing groups.

Galvanostatic discharge/charge measurements were performed across a wide range of current densities, from 50 to 6400 mA·g$^{-1}$, to evaluate the electrochemical performance of bilayer $Sn_4P_3$ electrodes (Figs. 4(a)–4(d)). As shown in Figs. 4(b) and 4(c), the bilayer $Sn_4P_3$ electrodes demonstrated an exceptionally high reversible capacity of 1084 mAh·g$^{-1}$ at 50 mA·g$^{-1}$. This capacity is remarkably close to the theoretical capacity of $Sn_4P_3$ (1230 mAh·g$^{-1}$) and surpasses those of three-layer (1059 mAh·g$^{-1}$), four-layer (1066 mAh·g$^{-1}$) $Sn_4P_3$ nanosheets, and bulk $Sn_4P_3$ (808 mAh·g$^{-1}$) (Fig. 4(d) and Figs. S13–S16 in the ESM), as well as previously reported $Sn_4P_3$-based anode materials [38–43]. With increasing the current density up to 800 mA·g$^{-1}$, the reversible capacity of the bilayer $Sn_4P_3$ remained impressively high at 570 mAh·g$^{-1}$, significantly exceeding the capacities of three-layer (489 mAh·g$^{-1}$), four-layer (353 mAh·g$^{-1}$) $Sn_4P_3$ nanosheets, and bulk $Sn_4P_3$ (144 mAh·g$^{-1}$). Furthermore, after 300 cycles at
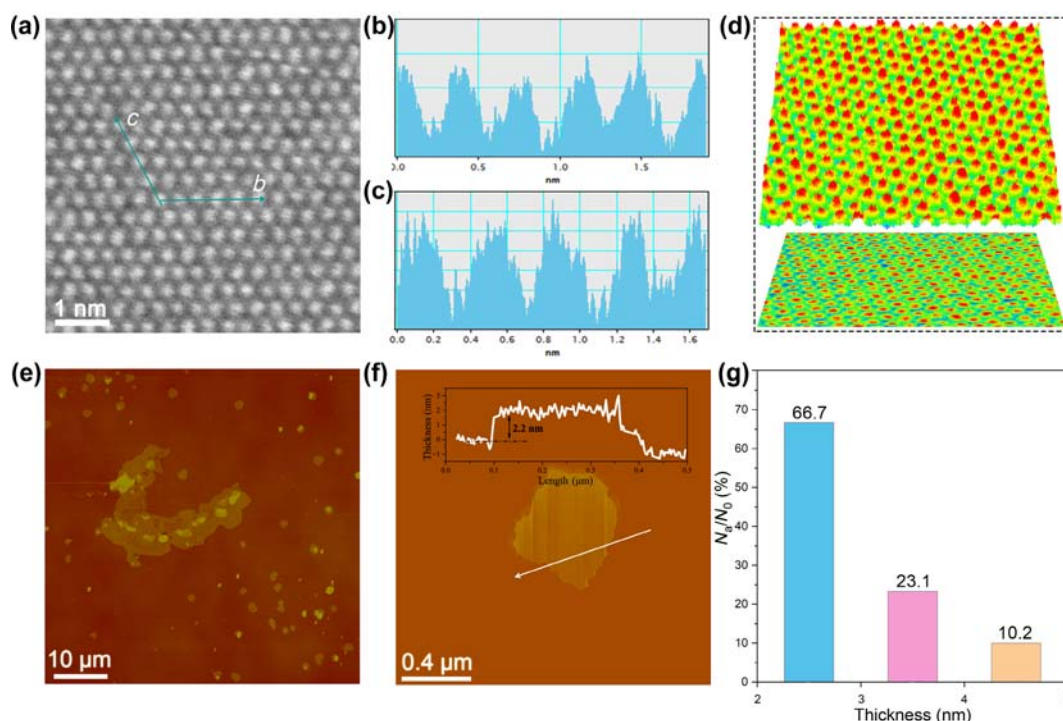


**Figure 2** (a) HAADF-STEM image of bilayer $Sn_4P_3$ nanosheets. (b) and (c) The surface atom profiles in (a). (d) Three-dimensional (3D) and 2D maps of bilayer $Sn_4P_3$ nanosheets in (a). (e) and (f) AFM images of bilayer $Sn_4P_3$ nanosheets. (g) The statistical diagram about the thickness of the bilayer $Sn_4P_3$ nanosheets based on (e), and Fig. S4 and Table S1 in the ESM.
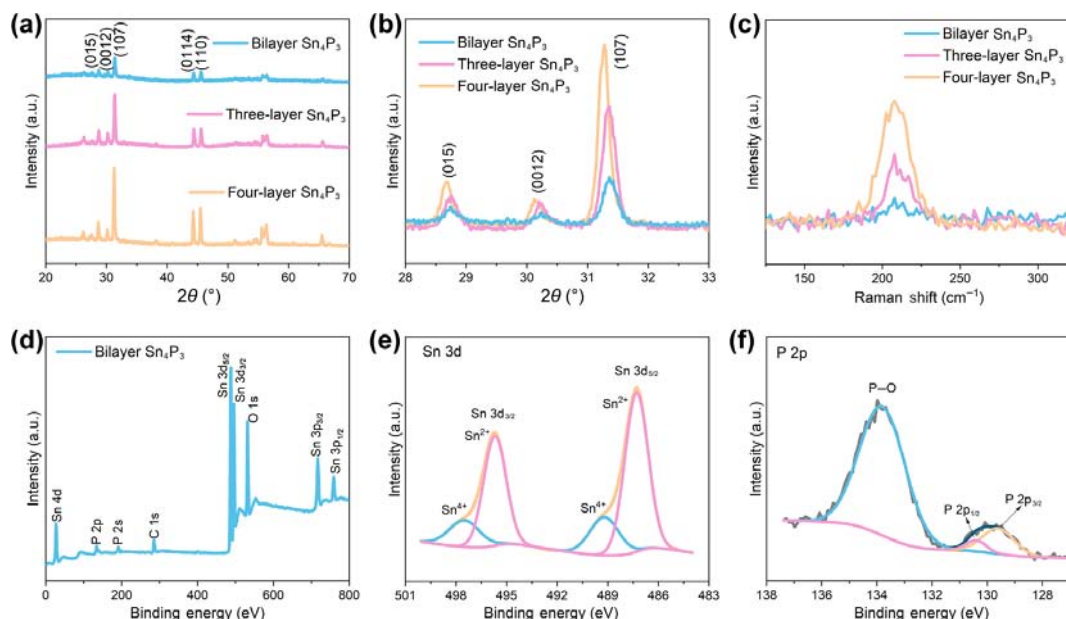
**Figure 3** (a) XRD patterns of bilayer, three-layer, and four-layer $Sn_4P_3$ nanosheets. (b) and (c) Raman spectra of bilayer, three-layer, and four-layer $Sn_4P_3$ nanosheets. (d) XPS spectra of bilayer $Sn_4P_3$ nanosheets. High resolution XPS spectra of (e) Sn 3d and (f) P 2p of bilayer $Sn_4P_3$ nanosheets.
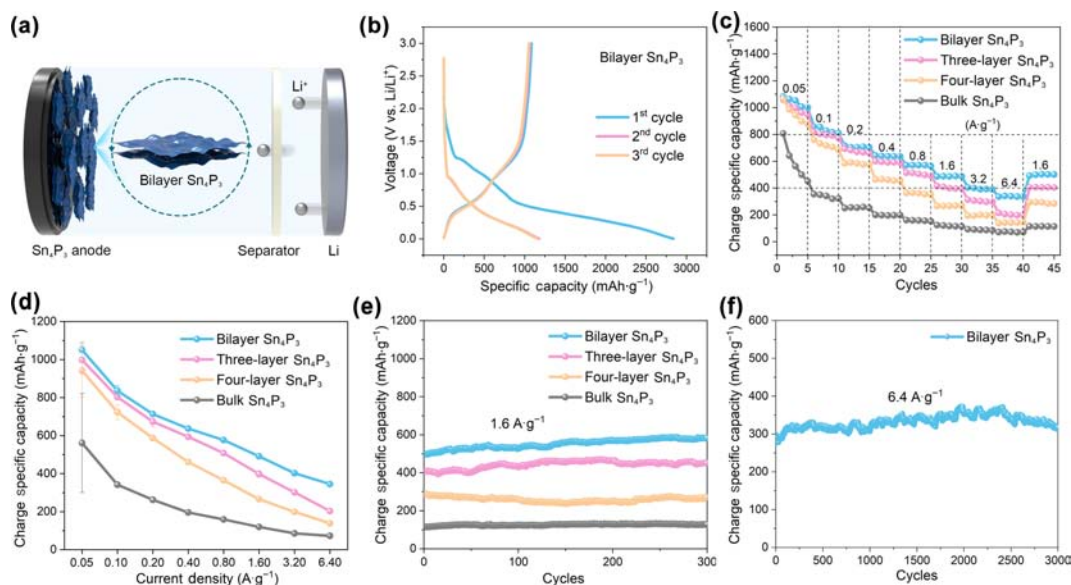


**Figure 4** (a) Schematic of $Sn_4P_3$ anode with Li counter electrode. (b) First-two charge–discharge curves of bilayer $Sn_4P_3$ nanosheets at the current density of 0.05 $A·g^{-1}$. (c) and (d) Rate performance of bilayer, three-layer, and four-layer $Sn_4P_3$ nanosheets and bulk $Sn_4P_3$ at various current density. (e) Cyclic performance of bilayer, three-layer, and four-layer $Sn_4P_3$ nanosheets and bulk $Sn_4P_3$ at the current density of 1.6 $A·g^{-1}$ for 300 cycles. (f) Ultralong cyclic performance of bilayer $Sn_4P_3$ nanosheets up to 1000 cycles at 6.4 $A·g^{-1}$.

1600 $mA·g^{-1}$, the reversible capacity of the bilayer $Sn_4P_3$ nanosheets remained stable at 586 $mAh·g^{-1}$ without any decay, as shown in Fig. 4(e). In comparison, three-layer, four-layer $Sn_4P_3$ nanosheets, and bulk $Sn_4P_3$ exhibited capacities of 450, 266, and 125 $mAh·g^{-1}$, respectively. Remarkably, the bilayer $Sn_4P_3$ nanosheets demonstrated an exceptional cycle life and stability, even when tested at the highest current density up to 6.4 $A·g^{-1}$. The bilayer $Sn_4P_3$ electrodes delivered an ultrahigh capacity of 330 $mAh·g^{-1}$ even after 1000 cycles (Fig. 4(f)). To the best of our knowledge, such outstanding electrochemical performance has never before been achieved by $Sn_4P_3$-based anodes, as summarized in Fig. 5(a) and Table S2 in the ESM. This exceptional electrochemical behavior underscores the significant potential of bilayer $Sn_4P_3$ nanosheets as anode materials for future energy storage applications.

To assess the lithium storage mechanism of bilayer $Sn_4P_3$ electrodes, cyclic voltammetry (CV) analysis was initially performed. Figure 5(b) illustrates the CV profiles of the first two

cycles for bilayer $Sn_4P_3$ nanosheets, conducted at 25 °C within a voltage range of 0.01 to 3 V. Notably, a broad peak at 1.08 V during the first discharge cycle indicates Li insertion into the bilayer $Sn_4P_3$ electrodes. Furthermore, two peaks observed around 0.75 and 0.09 V are attributed to the alloying of $Li_3P$ and $Li_xSn$. Subsequently, two peaks at 0.54 and 1.15 V appeared during the charge process, which should be attributed to the decomposition of $Li_xSn$ and $Li_3P$, respectively [40–42]. These findings are consistent with observations from three-layer, four-layer $Sn_4P_3$ nanosheets, and bulk $Sn_4P_3$ (Figs. S17–S19 in the ESM), and align with reported data on $Sn_4P_3$ electrodes. The typical charge–discharge curves of bilayer $Sn_4P_3$ electrodes, presented in Fig. 4(b), show distinct plateaus at ~ 0.5 and 1.0 V during the charging process. These plateaus correlate with the CV analysis and mirror the behavior observed in three-layer, four-layer $Sn_4P_3$ nanosheets, and bulk $Sn_4P_3$ (Figs. S20–S22 in the ESM), underscoring the high reversibility of the bilayer $Sn_4P_3$ electrodes. This high reversibility is attributed to the electrodes' unique
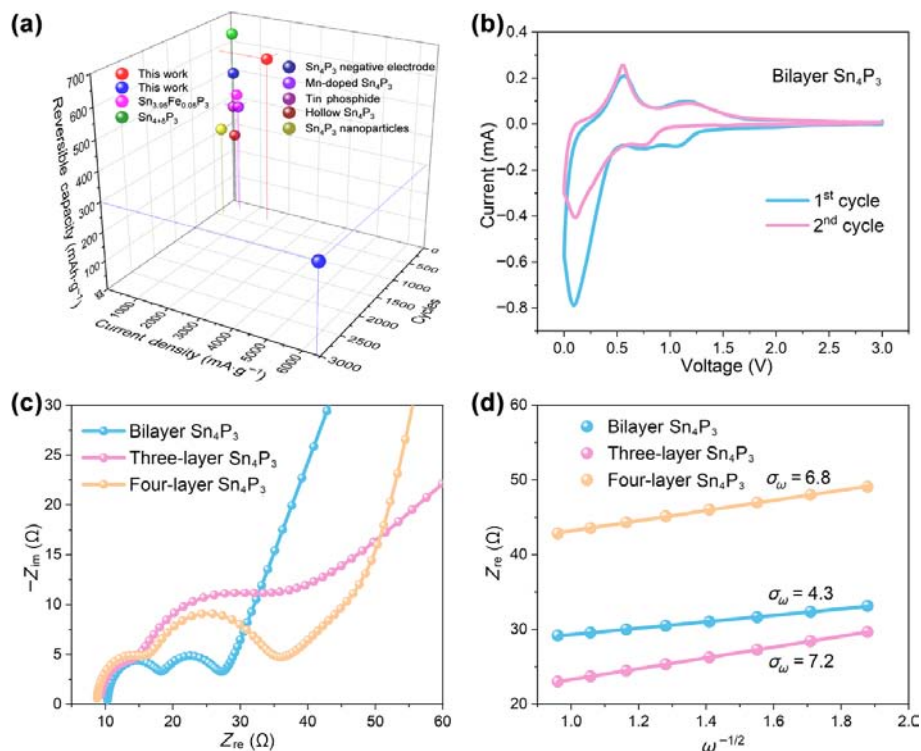
**Figure 5** (a) The comparison in electrochemical performance between our bilayer $Sn_4P_3$ nanosheets and some as-reported $Sn_4P_3$ anode materials. (b) CV curves of bilayer $Sn_4P_3$ nanosheets at the scan rate of 0.1 mV·s$^{-1}$. (c) Nyquist plots of bilayer, three-layer, and four-layer $Sn_4P_3$ nanosheets electrodes, respectively. (d) The relationship curve between $Z_{re}$ and $\omega^{-1/2}$ in the low-frequency region.

ultrathin layered structure, which plays a crucial role in enhancing their electrochemical performance.

To further elucidate the reasons behind the exceptional electrochemical performance of bilayer $Sn_4P_3$ electrodes, alternating-current (AC) impedance spectroscopy was performed after 500 cycles under consistent testing conditions. The Nyquist plot, as depicted in Fig. 5(c), was analyzed using a modified Randles equivalent circuit model (Fig. S23 in the ESM). This model incorporates a semicircle in the high-frequency range, representing the charge-transfer kinetic-controlled region, and a straight line in the low-frequency range, indicative of the mass transfer-controlled Warburg region.

The bilayer $Sn_4P_3$ electrodes exhibited a remarkably small $R_{ct}$ value of 8.7 Ω, much lower than those observed for three-layer $Sn_4P_3$ nanosheets (14.1 Ω), four-layer $Sn_4P_3$ nanosheets (16.0 Ω), and bulk $Sn_4P_3$ (19.9 Ω). Besides, from the relationship between $Z_{re}$ and $\omega^{-1/2}$, it can be concluded that bilayer $Sn_4P_3$ possesses a fast Li$^+$ diffusion than those of three-layer $Sn_4P_3$ and four-layer $Sn_4P_3$ anodes (Fig. 5(d)). This finding underscores the enhanced electrochemical performance of bilayer $Sn_4P_3$ electrodes compared to their thicker counterparts and bulk material, suggesting that the ultrathin bilayer structure substantially improves electrical conductivity. The substantially lower charge-transfer resistance of the bilayer $Sn_4P_3$ electrodes highlights their superior electrochemical kinetics, which is likely a key factor contributing to their excellent performance. This enhanced conductivity and reduced impedance facilitate more efficient lithium-ion transport and electron flow during the charge–discharge cycles, accounting for the high capacity, stability, and longevity observed in these electrodes. Thus, it is reasonable to conclude that the ultrathin bilayer $Sn_4P_3$ nanosheets markedly enhance the electrode's electrical conductivity, playing a crucial role in their good electrochemical performance.

## 4 Conclusions

In conclusion, we have successfully synthesized ultrathin bilayer $Sn_4P_3$ nanosheets via space-confined topochemical transformation strategy. By carefully adjusting the rolling number during the processing of Sn/Al foils, the number of $Sn_4P_3$ layer can be precisely controlled. Remarkably, the bilayer $Sn_4P_3$ nanosheets display an exceptional initial capacity of 1088 mAh·g$^{-1}$ as well as outstanding cycle life, maintaining capacity without fading more than 3000 cycles. By precisely controlling the layer thickness and ensuring nanoscale uniformity, we enhance the lithium cycling performance of $Sn_4P_3$, marking a significant advancement in the development of its practical application. These findings illuminate the profound potential of 2D nanomaterials in paving the way for the next generation of energy storage solutions, offering new perspectives on enhancing the efficiency and durability of electrochemical storage systems.

# References

[1] Zeng, L.; Tang, T. F.; Liang, Y. F.; Jiang, S. W.; Xu, X. T.; Wang, F. Molybdate-intercalated NiMn layered double hydroxide nanoarrays supercapacitor electrode with enhanced stability via a differentiated deposition strategy. *J. Power Sources* **2024**, *594*, 233990.

[2] Gu, J. N.; Shi, Y.; Du, Z. G.; Li, M. C.; Yang, S. B. Stress relief in metal anodes: Mechanisms and applications. *Adv. Energy Mater.* **2023**, *13*, 2302091.

[3] Gu, J. N.; Zhu, Q.; Shi, Y. Z.; Chen, H.; Zhang, D.; Du, Z. G.; Yang, S. B. Single zinc atoms immobilized on MXene ($Ti_3C_2Cl_x$) layers toward dendrite-free lithium metal anodes. *ACS Nano* **2020**, *14*, 891–898.

[4] Gu, J. N.; Chen, H.; Shi, Y.; Cao, Z. J.; Du, Z. G.; Li, B.; Yang, S. B. Eliminating lightning-rod effect of lithium anodes via sine-wave analogous MXene layers. *Adv. Energy Mater.* **2022**, *12*, 2201181.

[5] Kang, Q.; Li, Y.; Zhuang, Z. C.; Wang, D. S.; Zhi, C. Y.; Jiang, P. K.; Huang, X. Y. Dielectric polymer based electrolytes for high-performance all-solid-state lithium metal batteries. *J. Energy Chem.* **2022**, *69*, 194–204.

[6] Kang, Q.; Zhuang, Z. C.; Liu, Y. J.; Liu, Z. H.; Li, Y.; Sun, B.; Pei, F.; Zhu, H.; Li, H. F.; Li, P. L. et al. Engineering the structural uniformity of gel polymer electrolytes via pattern-guided alignment for durable, safe solid-state lithium metal batteries. *Adv. Mater.* **2023**, *35*, 2303460.

[7] Su, A. Y.; Apostol, P.; Wang, J. D.; Vlad, A.; Dincă, M. Electrochemical capacitance traces with interlayer spacing in two-dimensional conductive metal-organic frameworks. *Angew. Chem., Int. Ed.* **2024**, *63*, e202402526.

[8] Singh, M. K.; Krishnan, S.; Singh, K.; Rai, D. K. Effective assembling of nickel oxide-reduced graphene oxide heterostructures for ultrahigh capacity supercapattery. *J. Power Sources* **2024**, *595*, 234060.

[9] Liu, J. J.; Xing, G. L.; Chen, L. 2D conjugated metal-organic frameworks: Defined synthesis and tailor-made functions. *Acc. Chem. Res.* **2024**, *57*, 1032–1045.

[10] Cao, Z. J.; Zhang, Y. Z.; Cui, Y. L. S.; Gu, J. N.; Du, Z. G.; Shi, Y. Z.; Shen, K.; Chen, H.; Li, B.; Yang, S. B. Harnessing the unique features of 2D materials toward dendrite-free metal anodes. *Energy Environ. Mater.* **2022**, *5*, 45–67.

[11] Shi, Y. Z.; Li, B.; Zhang, Y. Z.; Cui, Y. L. S.; Cao, Z. J.; Du, Z. G.; Gu, J. N.; Shen, K.; Yang, S. B. Tortuosity modulation toward high-energy and high-power lithium metal batteries. *Adv. Energy Mater.* **2021**, *11*, 2003663.

[12] Zhu, H.; Sun, S. H.; Hao, J. C.; Zhuang, Z. H.; Zhang, S. G.; Wang, T. D.; Kang, Q.; Lu, S. L.; Wang, X. F.; Lai, F. L. et al. A high-entropy atomic environment converts inactive to active sites for electrocatalysis. *Energy Environ. Sci.* **2023**, *16*, 619–628.

[13] Zhuang, Z. C.; Kang, Q.; Wang, D. S.; Li, Y. D. Single-atom catalysis enables long-life, high-energy lithium-sulfur batteries. *Nano Res.* **2020**, *13*, 1856–1866.

[14] Kollipara, P. S.; Wu, Z. L.; Yao, K.; Lin, D. D.; Ju, Z. Y.; Zhang, X. T.; Jiang, T. Z.; Ding, H. R.; Fang, J.; Li, J. G. et al. Three-dimensional optothermal manipulation of light-absorbing particles in phase-change gel media. *ACS Nano* **2024**, *18*, 8062–8072.

[15] Kazim, S.; Huang, C.; Hemasiri, N. H.; Kulkarni, A.; Mathur, S.; Ahmad, S. MXene-based energy devices: From progressive to prospective. *Adv. Funct. Mater.*, in press, https://doi.org/10.1002/adfm.202315694.

[16] Hanan, A.; Lakhan, M. N.; Walvekar, R.; Khalid, M.; Prakash, C. Heteroatom-doped MXenes as electrocatalysts for hydrogen evolution reaction: A review on the recent advances, mechanisms and prospects. *Chem. Eng. J.* **2024**, *483*, 149107.

[17] Hanan, A.; Awan, H. T. A.; Bibi, F.; Sulaiman, R. R. R.; Wong, W. Y.; Walvekar, R.; Singh, S.; Khalid, M. MXenes and heterostructures-based electrocatalysts for hydrogen evolution reaction: Recent developments and future outlook. *J. Energy Chem.* **2024**, *92*, 176–206.

[18] Du, Z. G.; Guo, Y.; Wang, H. Y.; Gu, J. N.; Zhang, Y. Z.; Cheng, Z. J.; Li, B.; Li, S. M.; Yang, S. B. High-throughput production of 1T

[19] Chen, H.; Cao, Z. J.; Gu, J. N.; Cui, Y. L. S.; Zhang, Y. Z.; Zhao, Z. H.; Cheng, Z. J.; Zhao, Q.; Li, B.; Yang, S. B. Creating new battery configuration associated with the functions of primary and rechargeable lithium metal batteries. *Adv. Energy Mater.* **2021**, *11*, 2003746.

[20] Guo, T. Z.; Li, X.; Zhou, H. W.; Pang, L. X.; Zhou, T.; Shi, Z. Q.; Zhou, D. Effect of large-sized hydrophilic polypyrrole on electrochemical properties of MXene films. *J. Power Sources* **2024**, *593*, 233978.

[21] Grebenchuk, S.; McKeever, C.; Grzeszczyk, M.; Chen, Z. L.; Šiškins, M.; McCray, A. R. C.; Li, Y.; Petford-Long, A. K.; Phatak, C. M.; Ruihuan, D. et al. Topological spin textures in an insulating van der Waals ferromagnet. *Adv. Mater.* **2024**, *36*, 2311949.

[22] Das, P.; Marvi, P. K.; Ganguly, S.; Tang, X. W.; Wang, B.; Srinivasan, S.; Rajabzadeh, A. R.; Rosenkranz, A. MXene-based elastomer mimetic stretchable sensors: Design, properties, and applications. *Nano-Micro Lett.* **2024**, *16*, 135.

[23] Mansouri, Z.; Yaden, A.; El Manjli, F.; Ben Ali, M.; Tiouitchi, G.; Naamane, S.; Mounkachi, O.; El Maalam, K. Peering into recent advances in passivation strategies of few-layer black phosphorene toward battery anodes: A review. *J. Power Sources* **2023**, *587*, 233719.

[24] Gu, J. N.; Lv, Y. L.; Wang, Y. H.; Liu, L. H.; Li, M. C. Reconstructing 2D metallic $Sn_4P_3$ with high-conductive interlayer towards high-rate lithium storage. *Electrochim. Acta* **2024**, *480*, 143933.

[25] Gu, J. N.; Du, Z. G.; Zhang, C.; Ma, J. G.; Li, B.; Yang, S. B. Liquid-phase exfoliated metallic antimony nanosheets toward high volumetric sodium storage. *Adv. Energy Mater.* **2017**, *7*, 1700447.

[26] Kwon, N. H.; Yun, S. Y.; Lim, J.; Hwang, S. J. Recent advances in high-performance catalysts hybridized with two-dimensional conductive inorganic nanosheets. *Nano Energy* **2024**, *122*, 109315.

[27] Bu, Y. J.; Cabulong, R. B.; Kim, B. S. Plant extract-based liquid phase exfoliation enables one-step green production of two-dimensional heterostructure nanohybrids capable of dramatic improvement in polymer properties. *Green Chem.* **2024**, *26*, 3488–3506.

[28] Wang, P.; Zhao, Y.; Na, R.; Dong, W. K.; Duan, J. Y.; Cheng, Y.; Xu, B. Y.; Kong, D. N.; Liu, J. J.; Du, S. et al. Chemical vapor deposition synthesis of intrinsic high-temperature ferroelectric 2D $CuCrSe_2$. *Adv. Mater.* **2024**, *36*, 2400655.

[29] Tian, S.; Wang, W. J.; Zhao, M. F.; Han, Y. L.; Tian, Y. X.; Ji, S. X.; Yao, L.; Liu, L. X.; Ling, F. F.; Jia, Z. Y. et al. Room-temperature ferromagnetic $CoSe_2$ nanoplates synthesized by chemical vapor deposition. *J. Phys.: Condens. Matter* **2024**, *36*, 135802.

[30] Han, Z. Y.; Han, X. C.; Wu, S. Q.; Zhang, Q.; Hu, W. C.; Meng, Y.; Liang, Y.; Hu, J. Y.; Li, L.; Zhang, Q. et al. Phase and composition engineering of self-intercalated 2D metallic tantalum sulfide for second-harmonic generation. *ACS Nano* **2024**, *18*, 6256–6265.

[31] Ghorai, S.; Rajan, A. G. From molecular precursors to $MoS_2$ monolayers: Nanoscale mechanism of organometallic chemical vapor deposition. *Chem. Mater.* **2024**, *36*, 2698–2710.

[32] Lyu, X. Y.; Wu, G. H.; Zheng, Z. Y.; Xia, S. X.; Xie, J. Y.; Xia, Y.; Fan, P. S.; Zhu, R.; Wang, Y. J.; Yang, D. et al. Molecularly confined topochemical transformation of MXene enables ultrathin amorphous metal-oxide nanosheets. *ACS Nano* **2024**, *18*, 2219–2230.

[33] Zhu, Y. W.; Deng, W. F.; Tan, Y. M.; Shi, J. Q.; Wu, J. C.; Lu, W. B.; Jia, J. F.; Wang, S. Y.; Zou, Y. Q. *In situ* topochemical transformation of $ZnIn_2S_4$ for efficient photocatalytic oxidation of 5-hydroxymethylfurfural to 2,5-diformylfuran. *Adv. Funct. Mater.* **2023**, *33*, 2304985.

[34] Handy, J. V.; Andrews, J. L.; Perez-Beltran, S.; Powell, D. R.; Albers, R.; Whittaker-Brooks, L.; Bhuvanesh, N.; Banerjee, S. A "Li-eye" view of diffusion pathways in a 2D intercalation material from topochemical single-crystal transformation. *ACS Energy Lett.* **2022**, *7*, 1960–1962.

[35] Deng, Y. W.; Xi, X. Y.; Xia, Y.; Cao, Y. F.; Xue, S. Q.; Wan, S. Y.; Dong, A. G.; Yang, D. 2D FeP nanoframe superlattices via

MoS$_2$ monolayers based on controllable conversion of Mo-based MXenes. *ACS Nano* **2021**, *15*, 19275–19283.

space-confined topochemical transformation. *Adv. Mater.* **2022**, *34*, 2109145.

[36] Xiao, X.; Wang, H.; Urbankowski, P.; Gogotsi, Y. Topochemical synthesis of 2D materials. *Chem. Soc. Rev.* **2018**, *47*, 8744–8765.

[37] Gu, J. N.; Li, B.; Du, Z. G.; Zhang, C.; Zhang, D.; Yang, S. B. Multi-atomic layers of metallic aluminum for ultralong life lithium storage with high volumetric capacity. *Adv. Funct. Mater.* **2017**, *27*, 1700840.

[38] Liu, J.; Kopold, P.; Wu, C.; van Aken, P. A.; Maier, J.; Yu, Y. Uniform yolk–shell $Sn_4P_3$@C nanospheres as high-capacity and cycle-stable anode materials for sodium-ion batteries. *Energy Environ. Sci.* **2015**, *8*, 3531–3538.

[39] Liu, S. L.; Zhang, H. Z.; Xu, L. Q.; Ma, L. B.; Hou, X. High lithium storage performance of Mn-doped $Sn_4P_3$ nanoparticles. *Electrochim. Acta* **2016**, *210*, 888–896.

[40] Choi, J.; Kim, W. S.; Kim, K. H.; Hong, S. H. $Sn_4P_3$-C nanospheres as high capacitive and ultra-stable anodes for sodium ion and lithium ion batteries. *J. Mater. Chem. A* **2018**, *6*, 17437–17443.

[41] Luis Gomez-Camer, J.; Acebedo, B.; Ortiz-Vitoriano, N.; Monterrubio, I.; Galceran, M.; Rojo, T. Unravelling the impact of electrolyte nature on $Sn_4P_3$/C negative electrodes for Na-ion batteries. *J. Mater. Chem. A* **2019**, *7*, 18434–18441.

[42] Xia, Y.; Han, S. B.; Zhu, Y. M.; Liang, Y. Y.; Gu, M. Stable cycling of mesoporous $Sn_4P_3$/$SnO_2$@C nanosphere anode with high initial coulombic efficiency for Li-ion batteries. *Energy Storage Mater.* **2019**, *18*, 125–132.

[43] Yadav, P.; Malik, W.; Dwivedi, P. K.; Jones, L. A.; Shelke, M. V. Electrospun nanofibers of tin phosphide ($SnP_{0.94}$) nanoparticles encapsulated in a carbon matrix: A tunable conversion-cum-alloying lithium storage anode. *Energy Fuels* **2020**, *34*, 7648–7657.